SOLAR CELLS

Limiting phosphonic acid interlayer–perovskite reactivity to stabilize perovskite solar modules

Chengbin Fei, Yadong Zhang, Mengru Wang, Yuqian Yang, Xiaoqiang Shi, Shaojie Wang, Huanxin Guo, Chuanhang Guo, He Liu, Mingze Li, Hangyu Gu, Stephen Barlow, Wei You, Mengen Wang, Seth R. Marder, Jinsong Huang*

Full article and list of author affiliations:
https://doi.org/10.1126/science.adz7969

INTRODUCTION: Metal halide perovskite solar cells combine high power conversion efficiencies with pathways to low-cost manufacturing. A critical element in perovskite solar cells is the hole-transport layer, which extracts positive charges generated by light. Phosphonic acid–based self-assembled monolayers (PA-SAMs) are widely used to enhance initial device performance. However, ensuring long-term module stability under realistic operating conditions—particularly under the combined stresses of elevated temperature and full-spectrum illumination, including ultraviolet (UV) light—remains a major challenge that limits commercialization.

RATIONALE: Our investigation was motivated by the broader observation that perovskite solar cells incorporating most PA-SAMs often fail high-temperature (85°C) light-soaking stability tests, despite improving initial device efficiency. We also observed accelerated degradation when PA-SAMs were blended into the perovskite as a means to omit the hole-transport layer. We hypothesized that this instability arises from chemical reactions between the perovskite and the PA-SAMs. Specifically, if phosphonic acid groups are not firmly anchored to the transparent conductive oxide (TCO), they may react with constituents of the metal halide perovskite, initiating interfacial degradation. Accordingly, we reasoned that designing molecules that form exceptionally strong bonds to the substrate would suppress such reactivity and enhance device longevity, given that UV irradiation can cleave weak PA-SAM–TCO bonds.

RESULTS: We first conducted a systematic study and verified detrimental chemical reactions between PA-SAMs and perovskites. Using solution-state nuclear magnetic resonance spectroscopy and x-ray diffraction, we found that PA-SAM molecules oxidized iodide, decomposed the formamidinium cation, and reduced Pb to metallic lead. These reactions accelerate markedly at elevated temperature and under UV illumination. To quantify weak anchoring of PA-SAMs to TCOs, we developed a characterization workflow that combined mild acid washing with electrochemical and surface analyses. This revealed that ~30% of molecules in commonly used PA-SAMs are bound to TCO primarily through weak hydrogen bonds, making them prone to detachment during operation. To address this, we designed and synthesized a triphenylamine-based phosphonic acid (1PA-TPD) engineered for robust, covalent attachment to a TCO. Perovskite solar cells incorporating an optimized mixture of this strongly TCO-binding PA-SAM and a complementary one with strong affinity to the perovskite exhibited enhanced film crystallinity and reduced defect density. Under continuous operation at 85°C with full-spectrum illumination, these devices retained 90% of their initial efficiency (T_{90}) for nearly 3000 hours, substantially outperforming controls. For scale-up, we fabricated minimodules (aperture area >20 cm^2) that achieved >22% power conversion efficiency and a T_{90} of ~2200 hours under the same harsh conditions.

CONCLUSION: We identified and addressed a previously underappreciated degradation pathway in perovskite photovoltaics: reactions between PA-SAMs and the perovskite under simultaneous light and heat. By designing a molecule that forms a strongly anchored monolayer, we minimized the exposure of reactive acidic groups at the interface. This strategy delivers perovskite cells and modules with exceptional operational stability, marking a substantive step toward the reliability that is needed for commercial deployment. ☐

---

*Corresponding author. Email: jhuang@unc.edu Cite this article as C. Fei *et al.*, *Science* **391**, eadz7969 (2026). DOI: 10.1126/science.adz7969

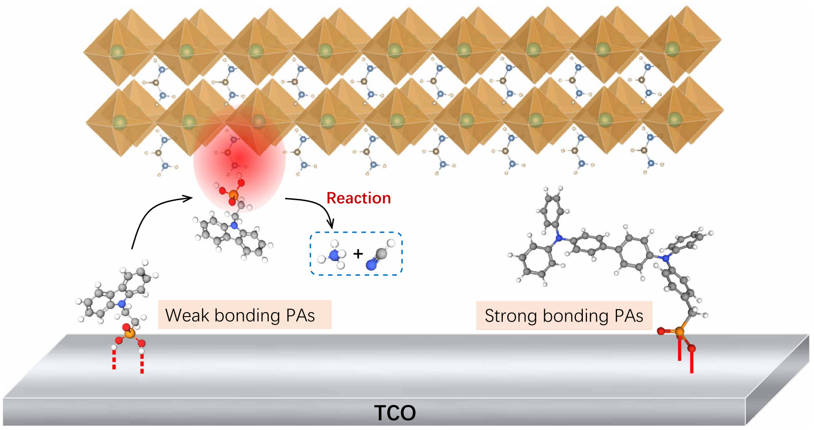

Reducing reaction at the PA-SAM–perovskite interface through stronger molecular anchoring. Weakly bonded phosphonic acids (PAs; lower left) can readily detach from the TCO substrate and leave reactive anchoring groups exposed and prone to reacting with perovskite components. By contrast, 1PA-TPD (lower right) establishes robust anchoring to the substrate, suppressing detachment and interfacial reactions and thereby improving device stability under realistic operating conditions. Colors in the ball-and-stick models are as follows: white, hydrogen; gray, carbon; blue, nitrogen; red, oxygen; orange, phosphorus.

SOLAR CELLS

Limiting phosphonic acid interlayer-perovskite reactivity to stabilize perovskite solar modules

Chengbin Fei[1], Yadong Zhang[2], Mengru Wang[1], Yuqian Yang[1], Xiaoqiang Shi[1], Shaojie Wang[1], Huanxin Guo[1], Chuanhang Guo[1], He Liu[1], Mingze Li[1], Hangyu Gu[1], Stephen Barlow[2], Wei You[1,3], Mengen Wang[4], Seth R. Marder[2,5,6], Jinsong Huang[1,3]*

Phosphonic acid (PA)–based interlayers used in metal-halide perovskite solar cells (PSCs) can suffer from instability at elevated temperatures. We report that the acidic protons of PAs weakly bound to indium tin oxide (ITO) can accelerate the oxidation of iodide, decomposition of formamidinium, and reduction of lead ions and that these reactions accelerate at high temperature and on exposure to ultraviolet light. Also, some common PA molecules weakly bonded to ITO can desorb and react with perovskites. We synthesized a bis(diarylamino) biphenyl-based PA that binds more strongly to ITO and show that its use in PSCs led to an operational lifetime of nearly 3000 hours with 10% efficiency loss (T_{90}) at 85°C under a metal halide lamp (including ultraviolet light) with maximum power point tracking. Minimodules had power conversion efficiencies >22% with an aperture area of >20 square centimeters and exhibited a T_{90} lifetime of ~2200 hours under similar testing conditions.

Perovskite solar cells (PSCs) have emerged as candidates for next-generation photovoltaics, offering certified power conversion efficiencies (PCEs) greater than 27%, low-cost fabrication, and tunable optoelectronic properties (*1*). The optimization of hole-transport materials (HTMs) remains critical to improving charge extraction, suppressing interfacial recombination, and enhancing device stability (*2*–*4*). Among HTMs, phosphonic acid (PA)–based hole-accepting molecules, often referred to as self-assembled monolayers (SAMs), offer facile synthesis, molecular-level design precision, and robust interfacial bonding (*5*–*8*). The typical carbazole-based PAs, such as [2-(9*H*-carbazol-9-yl)ethyl]phosphonic acid (2PACz) and [4-(3,6-dimethoxy-9*H*-carbazol-9-yl)butyl]phosphonic acid (Me-4PACz), enabled improvements in device PCE and durability by enhancing molecular coverage and minimizing nonradiative carrier recombination (*9*–*15*). [2-(9-Ethyl-9*H*-carbazol-3-yl)ethyl]phosphonic acid (EtCz3EPA) was developed to further strengthen binding to both the transparent conducting oxide (TCO) substrate and perovskites (*6*).

In many cases, the use of these PAs improves hole extraction, mitigates ultraviolet (UV)–induced interfacial damage, and enhances outdoor operational stability (*16*–*18*). Recent studies have shown that SAMs with ordered structures exhibit better stability when subject to external light and/or thermal stress, highlighting the importance of molecular stacking in device longevity (*19*–*23*). In addition, codeposition of SAMs with the perovskite layer can, in some cases, passivate grain boundaries and boost the initial PCEs (*24*–*26*). Despite these advances, there is no report of SAM-based perovskite modules continuously operating for >1000 hours under the combined stress of high temperature (≥85°C) and full-spectrum (with UV) light illumination. Some SAMs with weak binding to the TCO substrate undergo desorption under thermal or light-induced stress, which exacerbates interfacial degradation. The PAs can migrate into the interior of the perovskite layer, leading to a decrease in the level of device performance (*27*, *28*). Although SAMs can passivate the surface defects of the perovskite grains when the PA (or its conjugate base) is incorporated into the perovskite layer, deleterious effects can arise through interactions of the PA molecules and the cations in the perovskite layer.

We undertook a study to develop a deeper understanding of the role of acid (including the pK_a of the acid, where K_a is the acid dissociation constant) on the long-term stability of formamidinium (FA^+), iodide (I^-), and PSCs containing both ions. We found that the widely used PA-SAMs, although effective in improving the initial PCE, can, if desorbed from the indium tin oxide (ITO) substrate, react with perovskites. The rate of these reactions was accelerated at elevated temperatures and under exposure to UV light. Insights into the mechanism and rates of these chemical reactions were developed using nuclear magnetic resonance (NMR) spectroscopy and x-ray diffraction (XRD) analyses. We developed a new PA-SAM molecule that bound more strongly to ITO substrate relative to previous SAMs that we and others have examined. This strong binding inhibited detachment during perovskite deposition and operation. The perovskite minimodules with this PA-SAM as the HTM exhibited an improved operating PCE at high temperature and under full-spectrum illumination.

Reaction of PAs and perovskite under photothermal conditions

The PA molecules are often referred to as monolayers or SAMs when used as a hole transport layer (HTL), where their phosphonic group [$-PO(OH)_2$] bonds to TCO substrates. Reported binding modes include hydrogen bonding, as well as covalent metal-oxygen-phosphorus (M-O-P) linkages through one or two hydroxyl groups (*29*). In some cases, the phosphoryl oxygen (P=O) has been reported to participate in covalent interaction with the substrate, leading to tridentate binding modes (*30*–*32*). The specific binding mechanism of PAs depends on their structure and the deposition method, including the solvent and annealing procedure. Unfortunately, many deposition and annealing procedures that have been reported lack the necessary detail to enable comparison of the binding mode and ultimate surface coverage across laboratories.

To systematically evaluate whether the phosphonic group can react with perovskites, we incorporated EtCz3EPA as an additive into the $FA_{0.9}Cs_{0.1}PbI_3$ perovskite precursor solution and fabricated devices with the architecture ITO/EtCz3EPA/$FA_{0.9}Cs_{0.1}PbI_3$:EtCz3EPA/C_{60}/bathocuproine (BCP)/copper (Cu), where Cs is cesium and Pb is lead. In this configuration, EtCz3EPA served both as the HTM and as an additive within the perovskite layer, similar to previous reports (*24*). To exclude possible (but unlikely) reactions with the carbazole group, methyl PA (MPA), the simplest PA, was also used as an additive in identical device structures. The EtCz3EPA HTM was deposited by blade coating using a 1 mg ml^{-1} methanol solution at a speed of 20 mm s^{-1}. Methanol dried within 1 s, and we further annealed the PAs at 150°C for 5 min in air to promote the reaction. To minimize weakly bound species, the EtCz3EPA HTM layers were then intensively washed by methanol (≥10 times) before perovskite deposition. The stability of these devices was tested under accelerated aging conditions using a light-emitting plasma (LEP) lamp (100 mW cm^{-2}, ~2.2% UV, spectrum in fig. S1) at 85°C. As shown in fig. S2, devices containing either EtCz3EPA or MPA as additives within the perovskite layer exhibited higher initial PCEs than reference devices but showed faster degradation during a light-thermal test, suggesting a possible reaction of the PAs with perovskites.

To investigate the chemical reactions between PAs and perovskites, we first mixed PAs and formamidinium iodide (FAI) in deuterated dimethyl sulfoxide (DMSO-d_6) and examined the reaction products using ^{1}H-NMR spectroscopy. As shown in Fig. 1A and fig. S3, notable

---

[1]Department of Applied Physical Sciences, University of North Carolina at Chapel Hill, Chapel Hill, NC, USA. [2]Renewable and Sustainable Energy Institute, University of Colorado Boulder, Boulder, CO, USA. [3]Department of Chemistry, University of North Carolina at Chapel Hill, Chapel Hill, NC, USA. [4]Department of Physics and Astronomy, University of North Carolina at Chapel Hill, Chapel Hill, NC, USA. [5]Department of Chemistry, University of Colorado Boulder, Boulder, CO, USA. [6]Department of Chemical and Biological Engineering, University of Colorado Boulder, Boulder, CO, USA. ***Corresponding author. Email: jhuang@unc.edu**

changes in the NMR signals were observed after aging the FAI and MPA mixed solution at 85°C in air for 1 hour. Specifically, the $-NH_2$ peak from FA^+ [δ 8.81 parts per million (ppm)] split into two, one of which appeared as a doublet; the –OH peak of MPA shifted from δ 9.42 to δ 9.58 ppm; the –CH resonance of FA^+ (δ 7.78 to 7.93 ppm) evolved into a triplet of triplets; and the adventitious H_2O resonance (δ 3.36 ppm) was reduced and slightly shifted in the presence of MPA. The observation of a singlet NH and a singlet CH resonance from FA^+ under many conditions is caused by averaging of the couplings and the chemical inequivalence of N–H environments cis and trans to the adjacent C–H group by proton exchange with adventitious water (reversible deprotonation of FA^+); the spectra seen in the presence of MPA are consistent with suppression of this exchange by the PA and are consistent with spectra seen for FA^+ and substituted FA^+ derivatives in the presence of other strong Brønsted acids or of Lewis acids (*33–35*).

Additionally, a triplet signal with a 1:1:1 intensity ratio was detected at δ 6.95 to 7.25 ppm, characteristic of NH_4^+ formation (*36–38*). Repeating the experiment under a nitrogen atmosphere (fig. S4) revealed similar NH_4^+ peaks, ruling out oxidation by O_2 as the cause. When the heating time of the FAI-MPA mixture was extended to 100 hours, the –OH signal from MPA completely disappeared (fig. S4), accompanied by a marked increase in the NH_4^+ signal, confirming a chemical reaction between the phosphonic group of MPA and FA^+. This is shown by Reaction 1, thereby accelerating the subsequent degradation step under heating. Furthermore, additional tests were conducted by mixing FAI with other PAs or acids, including 2PACz, EtCz3EPA, boric acid (H_3BO_3), and acetic acid (AcOH). All mixtures exhibited NH_4^+ signals in the NMR spectra, suggesting that this degradation process is broadly applicable to a range of acidic species that contain –OH groups (R–OH) (fig. S5).

$$NH_2{-}CH{=}NH_2^+ + R{-}OH \rightleftharpoons NH_3^+{-}CH{=}NH_2^+ + R{-}O^-$$
$$\rightleftharpoons NH_3 + HCNH^+ \xrightarrow{\Delta} NH_4^+ + HCN\uparrow \tag{1}$$

A distinct color change was also observed in the FAI-MPA mixture solution after heating in air for 10 hours, whereas no color change occurred when heating was conducted under a nitrogen atmosphere. As shown in Fig. 1B, a notable absorption peak appeared around ~360 nm, characteristic of triiodide (I_3^-) (*39*, *40*), indicating the formation of I_2 and the oxidation of iodide (I^-). Quantitative analysis revealed that the I_3^- peak intensity in the FAI-MPA solution was ~73 times higher than that of the FAI-only solution when tested under identical conditions, suggesting that MPA promoted the oxidation reaction. Because no iodine formation was detected under nitrogen atmosphere, we assumed that the reaction between I^- and MPA proceeded as follows:

$$4H^+ + 4I^- + O_2 \rightarrow 2I_2 + 2H_2O \tag{2}$$

We also evaluated many other acids in terms of the capability in accelerating the oxidation of iodide, noting that oxygen in the presence of acid becomes a stronger oxidant. As shown in Fig. 1C, a clear negative correlation was observed between the amount of iodine formed and the pK_a values of the added acids; that is, molecules with stronger acidity (lower pK_a) exhibited greater reaction acceleration.

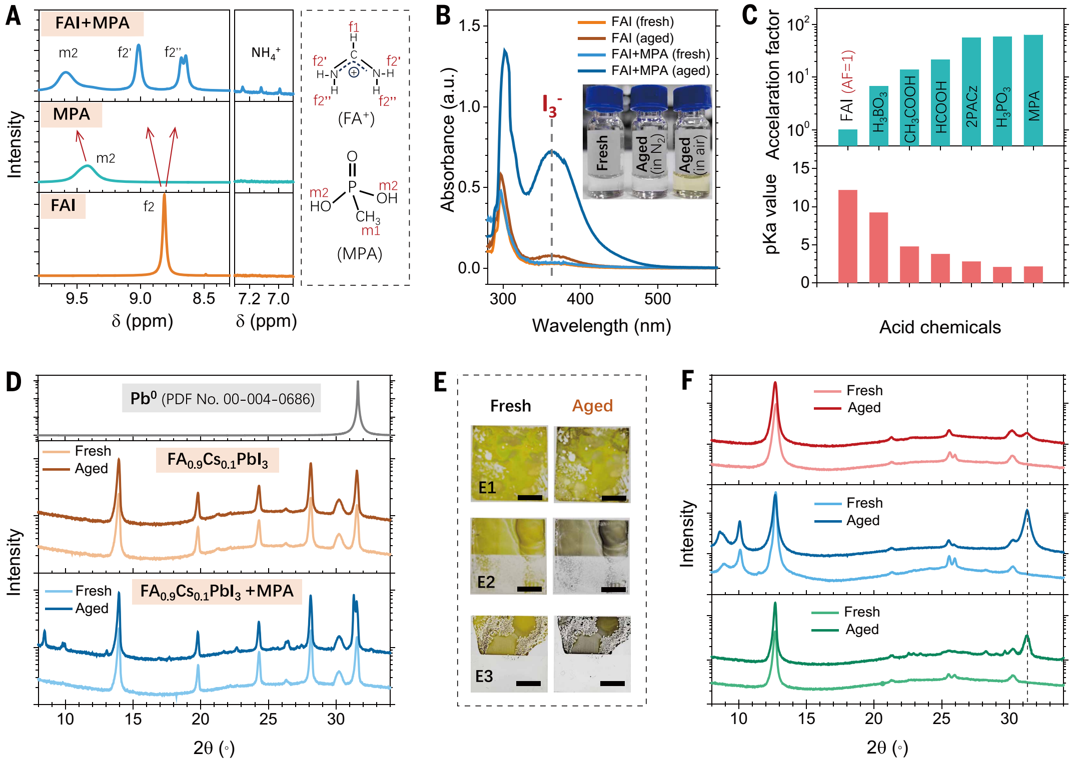

Fig. 1. Chemical reaction of PAs and perovskites. (**A**) ^{1}H-NMR of MPA, FAI, and the FAI-MPA mixture in DMSO-d_6. (**B**) UV-visible absorption spectrum of FAI and the FAI-MPA mixture (0.1M in DMSO-d_6) before and after 10 hours of aging (in air). The inset is a photograph of the FAI-MPA mixture solution before and after different aging conditions (in air or N_2). The aged solution of FAI-MPA for absorption test has been diluted by eight times for better comparison. a.u., arbitrary units. (**C**) The pK_a values and acceleration factors (AFs) of different acidic chemicals in the oxidation of I^-. The acceleration factor is determined by the ratio of I_2 formed, measured by the absorbance of the solution. (**D**) XRD patterns of the fresh and aged (85°C, 100 mW cm^{-2}, with 4.5% UV inside) $FA_{0.9}Cs_{0.1}PbI_3$ films with and without MPA (20% molar ratio to Pb^{2+}). The gray line represents a diffraction signal of Pb^0 [powder diffraction file (PDF) card: 00-004-0686]. (**E**) Photograph of the fresh and aged (85°C, 100 mW cm^{-2}, with 4.5% UV inside) PbI_2 films without addition (E1), with MPA (E2), and with HI (E3). The molar ratio of MPA and HI is 20% to Pb^{2+}. Scale bars are 5 mm. (**F**) The corresponding XRD patterns of the fresh and aged samples.

This finding directly supported the critical role of H^+ concentration in driving the oxidation of I^-.

To further investigate how PA molecules interact with perovskites in solid-state films, we fabricated $FA_{0.9}Cs_{0.1}PbI_3$ films mixed with MPA and aged them under a nitrogen atmosphere at 85°C for 120 hours using a metal halide (MH; 10,000K) lamp that closely replicates the UV proportion of the solar spectrum (fig. S2). As shown in Fig. 1D, the XRD patterns of the pristine $FA_{0.9}Cs_{0.1}PbI_3$ films exhibited barely any changes after aging. By contrast, films containing MPA displayed two additional low-angle peaks (≤10°), together with peak splitting around 31.5°, that agree with the diffraction peaks of metallic lead (Pb^0) (*41*). The presence of Pb^0 was further confirmed by dissolving the aged films in dimethyl sulfoxide (DMSO) to remove soluble components, yielding a gray solution and black precipitates (fig. S6). XRD analysis of the precipitate revealed peak positions matching Pb^0, confirming that Pb^{2+} was reduced to Pb^0 in the presence of MPA.

To elucidate how Pb^{2+} was reduced by MPA, we prepared PbI_2 films mixed with MPA to avoid the influence of other ions such as FA^+. These films were also aged under the same conditions. As shown in Fig. 1, E and F, PbI_2 films containing MPA turned black after 120 hours, with the intensity of the Pb^0 XRD peak being approximately five times higher than that of the control PbI_2 films. In addition, two distinct peaks appeared at 8.5° and 9.8°, which indicates the formation of phosphorus-lead compounds $CH_3PO_2(OH)PbI$ and CH_3PO_3Pb (fig. S7). This result shows that MPA accelerated the decomposition of PbI_2. Moreover, a rapid color change was observed only under MH lamp illumination, whereas the color change proceeded much more slowly under a white light-emitting diode (LED; <0.1% UV inside), suggesting that UV light accelerated the material decomposition (fig. S8).

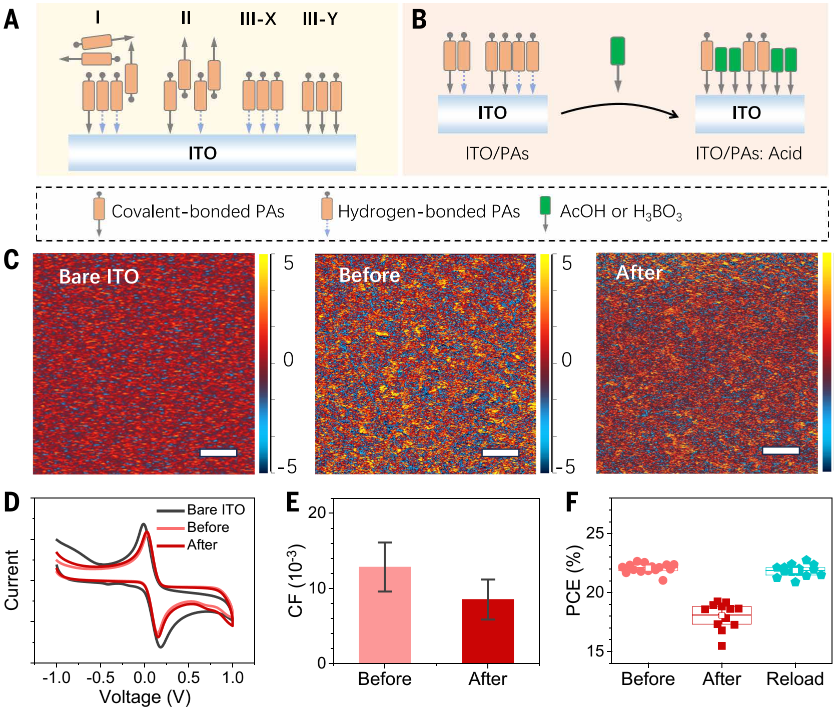

Fig. 2. Substitution of hydrogen-bonded PAs by acid. (**A**) Schematic illustration of different types of PA stacking modes on the ITO substrate. (**B**) Schematic of interfacial substitution of hydrogen-bonded PAs by acidic chemicals (AcOH or H_3BO_3). (**C**) AFM-IR spectra of ITO/EtCz3EPA samples before and after acid treatments. The IR images were collected around 1020 cm^{-1}, corresponding to C–H bending in $-CH_3$ groups of EtCz3EPA molecules. The bare ITO is measured as reference, and scale bars are 1 μm. (**D**) CV curves of ITO/EtCz3EPA samples before and after AcOH substitution. Ferrocene was added to the electrolyte. (**E**) Coverage factor (CF) of PAs before and after AcOH substitution. Error bars represent the standard deviation of data from 5 or 6 samples. (**F**) Efficiency evolution of devices fabricated on different substrates. The data were collected from 15 to 20 devices for each condition, and the active area of the small devices is 0.08 cm^2. The center line represents the median, box limits are upper and lower quartiles, and whiskers are the confidence interval.

Because CH_3PO_3Pb was generated from the reaction of MPA and PbI_2 (fig. S7), this reaction should also generate hydrogen iodide (HI), as shown in Reaction 3. We speculate that it could further react with PbI_2 to form H_xPbI_{2+x}, weakening the Pb–I bond and accelerating its decomposition under UV exposure. To verify this hypothesis, we prepared PbI_2 films mixed with HI solution and tested them under the same conditions. These films exhibited faster Pb^0 formation than the reference, although still slower than MPA-containing films, likely because of the effect of partial evaporation of HI during the heating process of film formation. The proposed mechanism by which MPA accelerates PbI_2 decomposition is summarized as follows:

$$CH_3PO(OH)_2 + PbI_2 \rightleftharpoons CH_3PO_2(OH)PbI + HI \rightleftharpoons CH_3PO_3Pb + 2HI \quad (3a)$$

$$xHI + PbI_2 \rightleftharpoons H_xPbI_{2+x} \xrightarrow{UV} xHI + Pb + I_2 \quad (3b)$$

Partial SAM detachment caused by weak hydrogen bonding

The interaction between exposed PA groups in SAMs and the perovskites under operational conditions has been identified as a key contributor to perovskite degradation. To mitigate this degradation pathway, it is essential to understand how SAM molecules orient themselves on the ITO surface, as their molecular configuration directly determines the extent of acid group exposure and interfacial reactivity. When PAs are deposited on ITO by a solution process without posttreatment, it is likely that some molecules form disordered multilayer structures (type I in Fig. 2A). In this configuration, the PA groups from the upper layers, represented by black arrows, are not anchored to ITO. These unbound molecules are readily dissolved by the perovskite precursor solution. Although solvent cleaning can partially remove these loosely adhered molecules, π-π interactions between the conjugated moieties (orange bars) often promote the formation of a bilayer structure (type II), as we observed for 2PACz. Although more stable, the exposed PA groups can react with perovskites at their interface. Type III refers to a well-defined monolayer configuration with the PA group anchored onto ITO. It is often assumed that SAM molecules are covalently bonded to the ITO surface. However, a subset may instead interact with ITO through hydrogen bonding (type III-X). These hydrogen-bonded molecules may temporarily survive solvent washing but can detach over time or under UV light, undermining long-term stability. The most desirable configuration is a fully covalently anchored monolayer (type III-Y), which offers the best stability.

To determine the percentage of those weakly bonded PAs, we conducted a washing process with diluted acid solution that could selectively substitute hydrogen-bonded PAs without affecting covalently bonded ones (Fig. 2B). We chose weak H_3BO_3 because we determined that it does not etch ITO (fig. S9). Atomic force microscopy–infrared (AFM-IR) spectroscopy mapping was used to characterize the coverage before and after acid washing. We monitored the IR absorption at a wave number of ~1020 cm^{-1}, which corresponds to the C–H bending vibration of $-CH_3$ groups (fig. S10). As shown in Fig. 2C, a distinct decrease in IR intensity was observed after H_3BO_3 treatment, indicating the removal of hydrogen-bonded SAM molecules. Similar results were observed for the widely used SAM molecule 2PACz (fig. S11), suggesting that those commonly used carbazole-based PAs are often only weakly bound to ITO and are thus susceptible to partial removal under weak acid treatment.

To further quantify the removal of EtCz3EPA molecules from the ITO surface, we performed cyclic voltammetry (CV) measurements before and after acetic acid (AcOH) treatment. We chose AcOH over H_3BO_3 because it was more easily removed by mild heating, thereby minimizing residual contamination on the substrate. After acid treatment, the substrates were annealed at 150°C for 3 min to ensure complete removal of residual AcOH. Bare ITO was used as a reference, and ferrocene was added to the electrolyte to provide a probe of the extent to which bare ITO is in electrical contact with the solution. Coating EtCz3EPA on ITO notably reduced the ferrocene signal, which we attributed to the blocking of active sites at the surface by the EtCz3EPA molecules (Fig. 2D). After acid treatment, the CV response increased substantially, indicating that some weakly bonded EtCz3EPA molecules were removed and that the electrode surface had regained electrochemical activity. Quantitative analysis suggested that ~29% of the EtCz3EPA molecules were removed by the acid treatment (table S1). X-ray photoelectron spectroscopy (XPS) data in Fig. 2E and fig. S12 show a ~32% reduction in SAM coverage based on the nitrogen-to-indium (N/In) elemental ratio. These results indicate that a portion of the monolayer, which we assume to be hydrogen-bonded PAs, can survive rigorous solvent washing but be detached by weak-acid treatment.

The loss of EtCz3EPA molecules through acid treatment had direct implications for device performance. Devices constructed on acid-treated substrates exhibited a 20% on average decrease in PCE compared with those fabricated on solvent-washed substrates (Fig. 2F). All substrates had undergone extensive solvent washing before acid treatment, underscoring that hydrogen-bonded PAs alone can influence device behavior. To validate the role of molecular coverage, we performed a second EtCz3EPA coating onto the acid-treated substrates, and the device efficiency was restored. This study provides direct evidence that the coverage of the PAs affected PCE.

Enhancing the bonding strength with triphenylamine-based PAs

We designed and synthesized a series of triphenylamine-based molecules with the molecular structures shown in Fig. 3A. Their synthesis and characterizations are described in the materials and methods and figs. S13 and S14. The triphenylamine core is known for its hole-transporting capability. These derivatives were designed to probe the influence of conjugation length and anchoring group chemistry on charge transport property and interfacial stability. These molecules were initially screened based on the efficiency and stability of devices. Among them, the device with (4-{[4′-(diphenylamino)-(1,1′-biphenyl)-4-yl](phenyl)amino}benzyl) phosphonic acid (1PA-TPD) demonstrated the best PCE and light thermal stability (fig. S15).

To experimentally validate the interaction strength between 1PA-TPD and the ITO substrate, AFM-IR spectroscopy images were obtained on ITO/1PA-TPD substrates before and after AcOH washing. As shown in Fig. 3B, AcOH washing led to no notable change in IR intensity, indicating minimal loss of SAM molecules. CV analysis (Fig. 3C and table S1) revealed that 11% of the 1PA-TPD molecules were removed by acid treatment, near the decrease in molecular coverage (~6%) determined by XPS (Fig. 3D and fig. S12). Furthermore, PSCs made with ITO/1PA-TPD substrate before and after acid treatment exhibited negligible differences in average PCEs (Fig. 3E). These results collectively support that 1PA-TPD forms strong anchoring interactions with ITO.

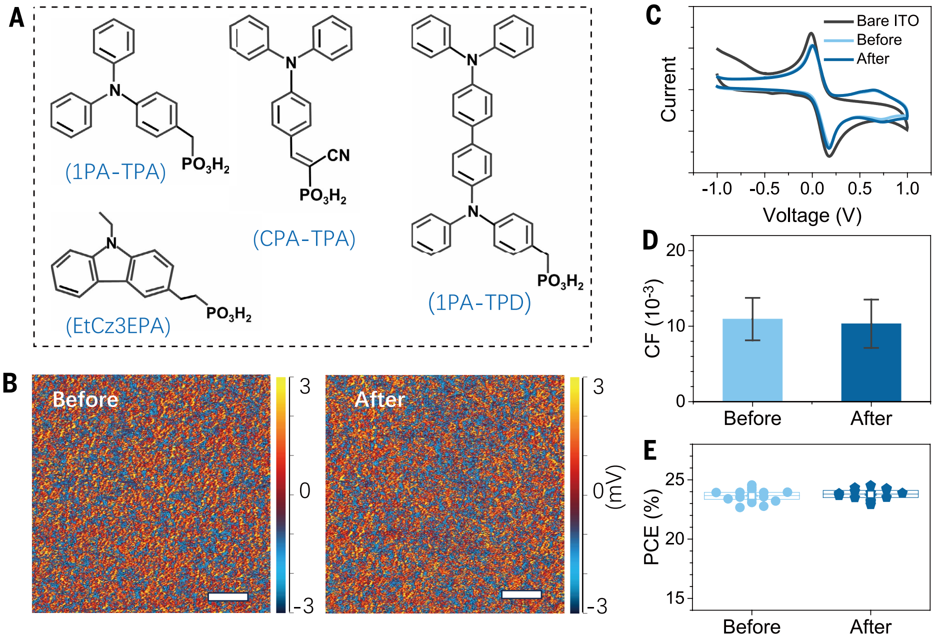

Fig. 3. Design of SAM molecules for robust bonding on ITO. (**A**) Molecular structure of triphenylamine-based PAs. (**B**) AFM-IR spectra of ITO/1PA-TPD samples before and after acid treatments. The IR images were collected around 1580 cm^{-1}, corresponding to C–C bending in benzene ring of 1PA-TPD. Scale bars are 1 μm. (**C**) CV curves of ITO/1PA-TPD samples before and after AcOH substitution. Ferrocene was added to the electrolyte. (**D**) Coverage factor of PAs before and after AcOH substitution. Error bars represent the standard deviation of data from 5 or 6 samples. (**E**) Efficiency evolution of devices fabricated on ITO/1PA-TPD substrates with and without AcOH substitution. The data were collected from 15 to 20 devices for each condition, and the active area of the small devices is 0.08 cm^2. The center line represents the median, box limits are upper and lower quartiles, and whiskers are confidence interval.

Improved photothermal stability of PSCs and minimodules

We used mixed PAs (40 wt % EtCz3EPA with 60 wt % 1PA-TPD), because 1PA-TPD, with its single PA anchoring group and sterically shielded triarylamine nitrogen, binds strongly to ITO but not to perovskites. This composition was optimized on the basis of the resulting device PCE and operation stability (fig. S16A). Before the perovskite deposition, the mixed PA-coated ITO substrates were intentionally washed with a solvent solution containing 5% AcOH to remove hydrogen-bonded PAs. PA deposition-washing cycles beyond two showed no further improvement (fig. S16B). Thereafter, perovskite films and devices fabricated with the mixed PAs of EtCz3EPA and 1PA-TPD as the HTM are referred to as "target," whereas those with the previously optimized hybrid HTM (EtCz3EPA/PTAA:BCP) are referred as "control" (*6*).

To evaluate the effect of the new HTM on perovskite crystallization, we obtained grazing incidence x-ray diffraction (GIXRD) data from the bottom side of perovskite films after peeling off the perovskite layer. The grazing incidence angle of 0.3° enabled a probing depth of ~50 nm into the film. Compared with the control sample, the target sample exhibited a ~50% increase in diffraction peak intensity and a narrower full width at half maximum by 0.02°, which was similar to EtCz3EPA-only–based samples as reported previously (*6*), indicating enhanced crystallinity (Fig. 4A). Time-resolved photoluminescence measured from the perovskite bottom side (without HTM) showed a carrier lifetime of 1.2 μs

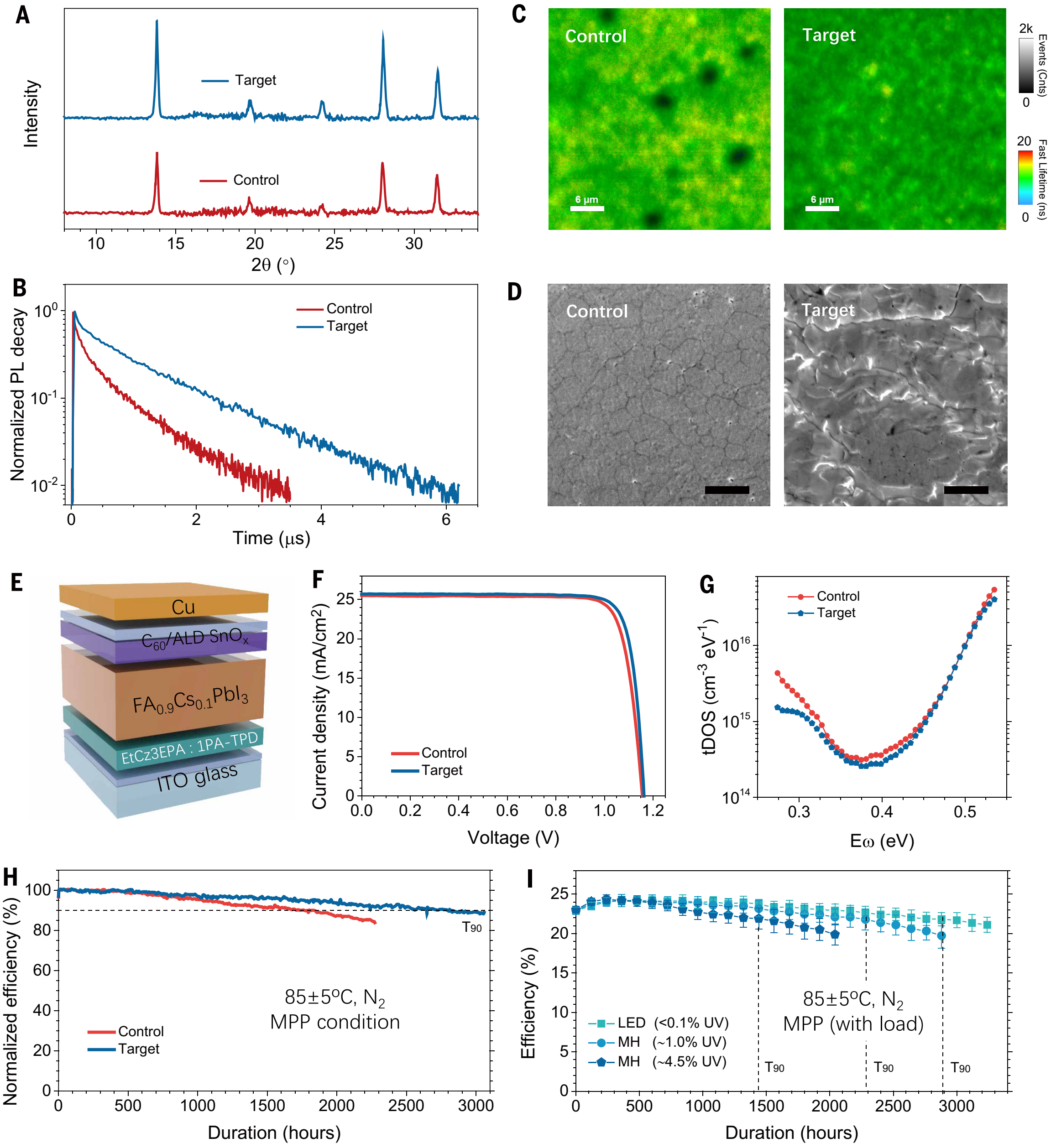

Fig. 4. Enhanced photothermal stability of PSCs. (**A**) GIXRD patterns of the fresh perovskite films prepared on different substrates. The samples were peeled off from ITO substrate and measured from the bottom perovskite side with an incident angle of 0.3°. (**B**) PL lifetime of the fresh perovskite films prepared on different substrates. (**C**) PL intensity and lifetime mapping images of aged samples collected from the ITO/HTM side of the samples. The aged samples were illuminated under a MH lamp and 85°C for ~500 hours (100 mW cm^{-2}, 4.5% UV inside). (**D**) SEM images of the control and target samples after peeling off. The samples were illuminated under a MH lamp and 85°C for ~500 hours (100 mW cm^{-2}, 4.5% UV inside). Scale bars are 2 μm. (**E**) Schematic of the configuration of small-area devices. (**F**) *J-V* curves of the PSCs with different HTMs. (**G**) Trap density of PSCs based on different substrates. E$_\omega$, demarcation energy; tDOS, total density of states. (**H**) Light-soaking stability of small-area devices (MPP conditions, 85° ± 5°C) based on different HTM layers under the illumination of a MH lamp (100 mW cm^{-2}, 1.0% UV inside). (**I**) Light-soaking stability of small-area devices (MPP conditions, with load, 85° ± 5°C) under different lamps. The active areas of the small devices are 0.08 cm^2, and the data were collected from 20 to 30 devices for each group.

for the target sample, ~2.6 times longer than that of the control (Fig. 4B), indicating lower deep-trap density in the perovskite layer.

To assess the influence of the new HTM on the long-term photothermal stability of perovskite, we analyzed the aged samples after 500 hours of operation with a MH lamp, under maximum power point (MPP) conditions at 85°C. The control devices showed localized dark regions in the photoluminescence (PL) mapping images (Fig. 4C), indicative of cation migration, phase segregation, or both. By contrast, the target devices exhibited minimal changes, suggesting greater stability under prolonged light and heat exposure.

We performed postaging peeling tests and imaged the bottom interface morphology with scanning electron microscopy (SEM) (Fig. 4D). Because of the presence of a PTAA layer above the EtCz3EPA in the control samples, the bottom surface of the perovskite layer appeared relatively flat with only minor pits. By contrast, the target sample exhibited a rough fracture surface, suggesting that the fracture occurred within the perovskite layer itself. Photographs of the peeled films (fig. S17) visually confirmed the formation of a robust ITO/HTM/perovskite interface in the target samples.

To gain deeper insight into the enhanced interfacial stability under photothermal stress, we performed a series of density functional theory calculations to evaluate the binding energies of 1PA-TPD and EtCz3EPA in both covalently bonded and hydrogen-bonded configurations. The covalently bonded structures considered two molecular orientations: single-molecule adsorption with an approximately parallel alignment to the surface and paired molecules adopting a more vertical geometry that enables intermolecular interactions. In both scenarios, 1PA-TPD exhibited higher binding energies than EtCz3EPA (see fig. S18). This is attributed to the formation of stronger In–O bonds between 1PA-TPD and the ITO substrate. In addition, the hydrogen-bonded configurations (fig. S19) also showed that the adsorption of 1PA-TPD was more stable than that of EtCz3EPA, mainly because of van der Waals interactions between 1PA-TPD and the ITO substrate.

We fabricated small-area PSCs incorporating different HTMs using the device architecture shown in Fig. 4E to assess their photovoltaic performance. In this configuration, the BCP layer was replaced by atomic layer–deposited tin oxide (ALD SnO_x), which offers an enhanced ability to retain light-induced iodine and effectively suppress Cu electrode diffusion (*42*). The control devices reached a PCE of 24.5% (Fig. 4F and table S2), matching values reported in previous studies (*6*), whereas the target devices achieved a slightly higher efficiency of 25.0%. To further probe the electronic properties of the devices, we analyzed the defect states within the perovskite layer. As shown in Fig. 4G, the target device exhibited a modest reduction in both trap band I (0.25 to 0.35 eV) and trap band II (0.35 to 0.45 eV), which correspond to negative (I_i^-) and positive (I_i^+) iodide interstitial defects, respectively (*43*, *44*). The measurement was taken from the fresh samples, and this reduction in trap states is aligned with the improvement of crystallinity of the perovskites. Impedance spectroscopy further confirmed this trend, showing clear interfacial degradation in the control device but only minor changes in the target device after aging (fig. S20).

We evaluated the photothermal stability of the devices under high-temperature and full-spectrum illumination conditions to accelerate degradation. We first determined the temperature coefficient of these devices. As shown in fig. S21, the temperature coefficient of the target devices is $-0.22\%\ ^\circ C^{-1}$, which outperforms the control device ($-0.29\%\ ^\circ C^{-1}$), making the target devices more efficient at high temperature.

We then measured the long-term operational stability of the unencapsulated devices under continuous illumination (100 mW cm^{-2}, 1.0% UV inside) at 85°C using MPP tracking systems in a N_2 filled glovebox. As shown in Fig. 4H and fig. S22, the control device reached 90% of its initial PCE (T_{90}) after ~1860 hours, whereas the target device exhibited a T_{90} lifetime of nearly 3000 hours, demonstrating that our molecular design strategy substantially enhances photothermal stability under realistic and accelerated test conditions. Considering that UV light accelerates interfacial reaction between PAs and perovskites, we further evaluated device stability under light sources with varying UV ratios. Specifically, the UV proportion of MH lamps increases with color temperatures, from 1.0% at 3200 K to 4.5% at 10,000 K. For each of the measurements, at least 10 devices were measured for each condition for statistical analysis. As shown in Fig. 4I and fig. S23, the T_{90} lifetimes were 2890, 2280, and 1430 hours for the devices illuminated by UV-free LED lamps, MH lamps with 1.0% UV, and MH lamps with 4.5% UV, respectively. Devices were connected with a fixed load to simulate the MPP condition and frequently transferred from a photothermal stability test setup to a current density–voltage (*J-V*) curve measurement system (in air). Notably, frequent *J-V* scans introduced additional bias stress, which may partially account for the shorter lifetimes that were observed compared with those under continuous MPP tracking, as shown in Fig. 4H (*45*, *46*). A slight reduction of conductivity from ITO electrodes was observed after these studies (fig. S24), and further study is needed to determine the contributions to the UV-related degradation from several different pathways such as ITO property changes, interfacial properties changes, and perovskite degradation.

Finally, we applied the HTMs to fabricate perovskite minimodules with an aperture area of ~23.1 cm^2. The best-performing module achieved a PCE of 22.1% at 25°C with no hysteresis, as shown in Fig. 5A and table S3. When the operating temperature increased to 85°C, the module PCE declined to 18.6%, corresponding to a temperature coefficient of $-0.26\%\ ^\circ C^{-1}$. An antireflection layer was used in this configuration and removed during the stability test.

To evaluate their long-term operational stability under elevated temperatures, we encapsulated the minimodules with polyisobutylene/polyolefin elastomer (Fig. 5B) (*47*). For accelerated photothermal aging, the modules were placed under large-area LEP lamps (100 mW cm^{-2}, with 2.2% UV) and were maintained at MPP conditions throughout the test. As shown in Fig. 5C and table S4, stability testing of four modules from two fabrication batches (indicated by green and blue lines) yielded an average T_{90} lifetime of ~1750 hours under continuous light illumination at 85°C. The best-performing module achieved a T_{90} of ~2200 hours, which represents a substantial advance in the durability of SAM-based perovskite modules under combined stress of high temperature and full-spectrum light (including UV).

Discussion

The PAs, which are widely used as HTMs in PSCs, can chemically interact with the perovskite under photothermal stress, accelerating its degradation. This detrimental reaction can be effectively suppressed by covalently anchoring a single layer of PAs to the ITO substrate, thereby reducing the interfacial exposure of reactive phosphonate groups. Notably, approximately one-third of conventional PAs remain removable from ITO by weak acid, presumably as a result of being noncovalently bound. To address this issue, we designed and synthesized a triphenylamine-based PA, 1PA-TPD, that features enhanced binding

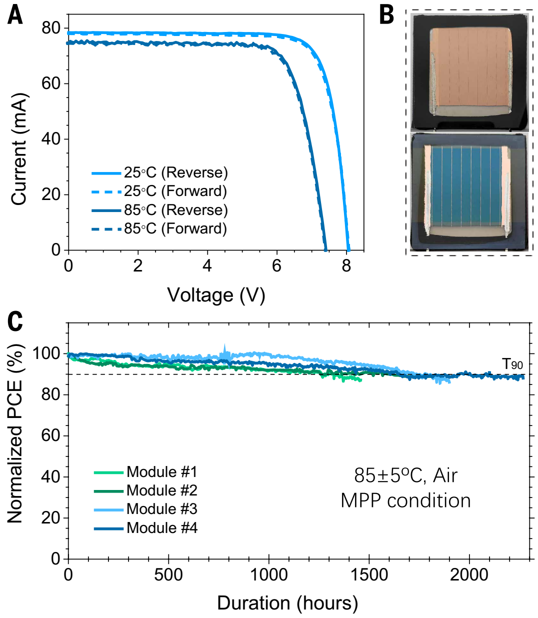

Fig. 5. Stabilized perovskite minimodules under photothermal conditions. (**A**) *J-V* curves of perovskite minimodules with new hybrid PAs as HTMs under different operation temperatures. (**B**) Photographs of the encapsulated perovskite minimodule viewed from the copper electrode side (top) and the ITO side (bottom). (**C**) Operational stability of perovskite minimodules under 85°C and a LEP lamp (100 mW cm^{-2}, with 2.2% UV inside). The aperture of the minimodules is ~23.1 cm^2.

affinity to ITO. PSCs incorporating this new PA and EtCz3EPA demonstrated a T_{90} operational lifetime of nearly 3000 hours under full-spectrum illumination at 85°C under MPP tracking. Furthermore, the best-performing minimodule exhibited a T_{90} approaching 2200 hours under the same conditions.

Materials and methods are available in the supplementary materials.

REFERENCES AND NOTES

1. National Renewable Energy Laboratory (NREL), Best research-cell efficiency chart (2025); https://www.nrel.gov/pv/cell-efficiency.html.
2. Y. Yao *et al.*, Organic hole-transport layers for efficient, stable, and scalable inverted perovskite solar cells. *Adv. Mater.* **34**, e2203794 (2022). doi: 10.1002/adma.202203794; pmid: 35771986
3. Y. An *et al.*, Balancing carrier transport in interconnection layer for efficient perovskite/organic tandem solar cells. *Nat. Commun.* **16**, 2759 (2025). doi: 10.1038/s41467-025-58047-3; pmid: 40113788
4. G. Yang *et al.*, Defect engineering in wide-bandgap perovskites for efficient perovskite–silicon tandem solar cells. *Nat. Photonics* **16**, 588–594 (2022). doi: 10.1038/s41566-022-01033-8
5. J. Tao *et al.*, Suppressing non-radiative recombination for efficient and stable perovskite solar cells. *Energy Environ. Sci.* **18**, 509–544 (2025). doi: 10.1039/D4EE02917H
6. C. Fei *et al.*, Strong-bonding hole-transport layers reduce ultraviolet degradation of perovskite solar cells. *Science* **384**, 1126–1134 (2024). doi: 10.1126/science.adi4531; pmid: 38843338
7. C. Shi *et al.*, Modulating competitive adsorption of hybrid self-assembled molecules for efficient wide-bandgap perovskite solar cells and tandems. *Nat. Commun.* **16**, 3029 (2025). doi: 10.1038/s41467-025-58111-y; pmid: 40155376
8. S. Lenaers *et al.*, Pyrene-based self-assembled monolayer with improved surface coverage and energy level alignment for perovskite solar cells. *Adv. Funct. Mater.* 2411922 (2024). doi: 10.1002/adfm.202411922
9. A. Al-Ashouri *et al.*, Monolithic perovskite/silicon tandem solar cell with >29% efficiency by enhanced hole extraction. *Science* **370**, 1300–1309 (2020). doi: 10.1126/science.abd4016; pmid: 33303611
10. H. Chen *et al.*, Improved charge extraction in inverted perovskite solar cells with dual-site-binding ligands. *Science* **384**, 189–193 (2024). doi: 10.1126/science.adm9474; pmid: 38603485
11. D. Li *et al.*, Co-adsorbed self-assembled monolayer enables high-performance perovskite and organic solar cells. *Nat. Commun.* **15**, 7605 (2024). doi: 10.1038/s41467-024-51760-5; pmid: 39218952
12. H. Zhou *et al.*, Rational design strategy of co-self-assembled monolayers for high-efficiency and stable inverted perovskite solar cells. *Chem. Eng. J.* **511**, 162010 (2025). doi: 10.1016/j.cej.2025.162010
13. S. Yu *et al.*, Homogenized NiO_x nanoparticles for improved hole transport in inverted perovskite solar cells. *Science* **382**, 1399–1404 (2023). doi: 10.1126/science.adj8858; pmid: 37995210
14. C. Guo *et al.*, Bifacially reinforced self-assembled monolayer interfaces for minimized recombination loss and enhanced stability in perovskite/silicon tandem solar cells. *Adv. Mater.* **37**, e2504520 (2025). doi: 10.1002/adma.202504520; pmid: 40351064
15. S. Ameen *et al.*, 3,6-Bis(methylthio)-9*H*-carbazole based self-assembled monolayer for highly efficient and stable inverted perovskite solar cells. *Angew. Chem. Int. Ed.* **64**, e202423206 (2025). doi: 10.1002/anie.202423206; pmid: 39663196
16. S. Qu *et al.*, Redox mediator-modified self-assembled monolayer stabilizes a buried interface in efficient inverted perovskite solar cells. *Energy Environ. Sci.* **18**, 3186–3195 (2025). doi: 10.1039/D4EE05319B
17. Y. Yao *et al.*, Oriented wide-bandgap perovskites for monolithic silicon-based tandems with over 1000 hours operational stability. *Nat. Commun.* **16**, 40 (2025). doi: 10.1038/s41467-024-55377-6; pmid: 39747820
18. W. Cheng *et al.*, Molecular bridging of buried interface flattens grain boundary grooves and imparts stress relaxation for performance enhancement and UV stability in perovskite solar cells. *Adv. Energy Mater.* **15**, 2501296 (2025). doi: 10.1002/aenm.202501296
19. G. Qu *et al.*, Self-assembled materials with an ordered hydrophilic bilayer for high performance inverted perovskite solar cells. *Nat. Commun.* **16**, 86 (2025). doi: 10.1038/s41467-024-55523-0; pmid: 39747047
20. Z. Zhang *et al.*, Synergistic improvement of structural ordering and interface binding of hole transport monolayer for efficient inverted perovskite solar cells. *Adv. Energy Mater.* **15**, 2500572 (2025). doi: 10.1002/aenm.202500572
21. B. Dong *et al.*, Self-assembled bilayer for perovskite solar cells with improved tolerance against thermal stresses. *Nat. Energy* **10**, 342–353 (2025). doi: 10.1038/s41560-024-01689-2
22. P. Hou *et al.*, Ordered self-assembled monolayer improved the buried interface of wide bandgap perovskite for efficient and stable semi-transparent solar cells. *Chem. Eng. J.* **503**, 158499 (2025). doi: 10.1016/j.cej.2024.158499
23. Y. Chang *et al.*, Highly oriented and ordered co-assembly monolayers for inverted perovskite solar cells. *Angew. Chem. Int. Ed.* **64**, e202418883 (2025). doi: 10.1002/anie.202418883; pmid: 39668652
24. X. Zheng *et al.*, Co-deposition of hole-selective contact and absorber for improving the processability of perovskite solar cells. *Nat. Energy* **8**, 462–472 (2023). doi: 10.1038/s41560-023-01227-6
25. Q. Tan *et al.*, Inverted perovskite solar cells using dimethylacridine-based dopants. *Nature* **620**, 545–551 (2023). doi: 10.1038/s41586-023-06207-0; pmid: 37224876
26. J. Suo, B. Yang, D. Bogachuk, G. Boschloo, A. Hagfeldt, The dual use of SAM molecules for efficient and stable perovskite solar cells. *Adv. Energy Mater.* **15**, 2400205 (2025). doi: 10.1002/aenm.202400205
27. H. Tang *et al.*, Reinforcing self-assembly of hole transport molecules for stable inverted perovskite solar cells. *Science* **383**, 1236–1240 (2024). doi: 10.1126/science.adj9602; pmid: 38484063
28. Z. Li *et al.*, Stabilized hole-selective layer for high-performance inverted p-i-n perovskite solar cells. *Science* **382**, 284–289 (2023). doi: 10.1126/science.ade9637; pmid: 37856581
29. S. P. Pujari, L. Scheres, A. T. M. Marcelis, H. Zuilhof, Covalent surface modification of oxide surfaces. *Angew. Chem. Int. Ed.* **53**, 6322–6356 (2014). doi: 10.1002/anie.201306709; pmid: 24849332
30. P. B. Paramonov *et al.*, Theoretical characterization of the indium tin oxide surface and of its binding sites for adsorption of phosphonic acid monolayers. *Chem. Mater.* **20**, 5131–5133 (2008). doi: 10.1021/cm8014622
31. W. Gao, L. Dickinson, C. Grozinger, F. G. Morin, L. Reven, Self-assembled monolayers of alkylphosphonic acids on metal oxides. *Langmuir* **12**, 6429–6435 (1996). doi: 10.1021/la9607621
32. C. Wood, H. Li, P. Winget, J.-L. Brédas, Binding modes of fluorinated benzylphosphonic acids on the polar ZnO surface and impact on work function. *J. Phys. Chem. C Nanomater. Interfaces* **116**, 19125–19133 (2012). doi: 10.1021/jp3050725
33. L. Chen *et al.*, Deciphering reaction products in formamidine-based perovskites with methylammonium chloride additive. *J. Am. Chem. Soc.* **145**, 27900–27910 (2023). doi: 10.1021/jacs.3c12755; pmid: 38078405
34. W. T. M. Van Gompel *et al.*, Degradation of the formamidinium cation and the quantification of the formamidinium-methylammonium ratio in lead iodide hybrid perovskites by nuclear magnetic resonance spectroscopy. *J. Phys. Chem. C Nanomater. Interfaces* **122**, 4117–4124 (2018). doi: 10.1021/acs.jpcc.7b09805
35. S. Zhou *et al.*, Reactive passivation of wide-bandgap organic-inorganic perovskites with benzylamine. *J. Am. Chem. Soc.* **146**, 27405–27416 (2024). doi: 10.1021/jacs.4c06659; pmid: 39348291
36. M. Kolen, W. A. Smith, F. M. Mulder, Accelerating ^1H NMR detection of aqueous ammonia. *ACS Omega* **6**, 5698–5704 (2021). doi: 10.1021/acsomega.0c06130; pmid: 33681609
37. W. Wang, D. Zhu, J. Luo, J. Zhu, X. Liu, Self-assembly of $(NH_4)_{0.3}TiO_{1.1}F_{2.1}$ crystal by dinitrogen fixation as a precursor of N-doped TiO_2 nanosheets. *J. Nanopart. Res.* **18**, 152 (2016). doi: 10.1007/s11051-016-3433-y
38. A. C. Nielander *et al.*, A versatile method for ammonia detection in a range of relevant electrolytes via direct nuclear magnetic resonance techniques. *ACS Catal.* **9**, 5797–5802 (2019). doi: 10.1021/acscatal.9b00358
39. H. Inoue, Y. Liang, T. Yamada, N. Kimizuka, Enhanced Seebeck coefficients of thermocells by heat-induced deposition of I_3^-/hydrophobized α-cyclodextrin complexes on electrodes. *Chem. Commun.* **56**, 7013–7016 (2020). doi: 10.1039/D0CC02356F; pmid: 32441729
40. S. V. Kireev, S. L. Shnyrev, Study of molecular iodine, iodate ions, iodide ions, and triiodide ions solutions absorption in the UV and visible light spectral bands. *Laser Phys.* **25**, 075602 (2015). doi: 10.1088/1054-660X/25/7/075602
41. M. Karbasi, E. Keshavarz Alamdari, E. Amirkhani Dehkordi, F. Tavangarian, Electrochemical and anodic behaviors of MnO_2/Pb nanocomposite in zinc electrowinning. *J. Appl. Electrochem.* **48**, 379–390 (2018). doi: 10.1007/s10800-018-1163-9
42. N. Li *et al.*, Barrier reinforcement for enhanced perovskite solar cell stability under reverse bias. *Nat. Energy* **9**, 1264–1274 (2024). doi: 10.1038/s41560-024-01579-7
43. Z. Ni *et al.*, Evolution of defects during the degradation of metal halide perovskite solar cells under reverse bias and illumination. *Nat. Energy* **7**, 65–73 (2022). doi: 10.1038/s41560-021-00949-9
44. C. Fei *et al.*, Lead-chelating hole-transport layers for efficient and stable perovskite minimodules. *Science* **380**, 823–829 (2023). doi: 10.1126/science.ade9463; pmid: 37228201
45. M. V. Khenkin, A. K.M., E. A. Katz, I. Visoly-Fisher, Bias-dependent degradation of various solar cells: Lessons for stability of perovskite photovoltaics. *Energy Environ. Sci.* **12**, 550–558 (2019). doi: 10.1039/C8EE03475C
46. D. Gupta *et al.*, Study of bias-induced degradation mechanism in perovskite $CH_3NH_3PbI_{3-x}Cl_x$ solar cells by electroluminescence spectroscopy. *Appl. Phys. A Mater. Sci. Process.* **129**, 127 (2023). doi: 10.1007/s00339-023-06407-5
47. H. Jiao *et al.*, Metal halide perovskite solar module encapsulation using polyolefin elastomers: The role of morphology in preventing delamination. *PRX Energy* **3**, 023013 (2024). doi: 10.1103/PRXEnergy.3.023013

ACKNOWLEDGMENTS

Funding: The study of chemical reaction is supported by the US Department of Energy (DOE), Office of Energy Efficiency and Renewable Energy (EERE), under the Solar Energy Technologies Office, award no. DE-EE0009520. The design and synthesis of PAs at the University of Colorado–Boulder was supported by the Office of Naval Research under award no. N00014-24-1-2115. The study of new PAs and module demonstration was supported by the

Office of Naval Research under award no. N6833522C0122 and the University of North Carolina (UNC) Research Opportunity Initiative. Computational resources were provided by Bridges-2 at the Pittsburgh Supercomputing Center through allocation no. MAT230043 from the Advanced Cyberinfrastructure Coordination Ecosystem: Services & Support (ACCESS) program, which is supported by National Science Foundation grants 2138259, 2138286, 2138307, 2137603, and 2138296 and the Theory and Computation facility of the Center for Functional Nanomaterials (CFN) and the Scientific Data and Computing Center at Brookhaven National Laboratory under contract no. DE-SC0012704. The views expressed here do not necessarily represent the views of the US DOE or the US government. **Author contributions:** C.F. and J.H. conceived the idea. C.F. fabricated and characterized perovskite films and devices. S.R.M., Y.Z., and S.B. designed the new PAs, and Y.Z. synthesized and characterized the PAs. Mengr.W. performed the GIXRD measurements, acquired the SEM images, and carried out the tDOS analysis. X.S. optimized the module encapsulation. S.W. and C.G. carried out the AFM-IR and AFM measurements and analyses. Hu.G. performed the NMR studies. H.L. carried out the PL mapping of the samples. Y.Y. and W.Y. carried out the CV tests. M.L. performed the regular XRD test. Menge.W. performed the density functional theory calculations. Ha.G. performed the UV-visible absorption measurements. C.F. and J.H. wrote the manuscript, and all authors commented on the manuscript. **Competing interests:** C.F. and J.H. are authors of a provisional patent (application no. 63/875,395) based on this manuscript. J.H. discloses financial interests with Perotech, Inc. These relationships have been disclosed to and are under management by University of North Carolina–Chapel Hill. The authors declare no other competing interests. **Data, code, and materials availability:** All data are available in the main text or the supplementary materials. **License information:**

SUPPLEMENTARY MATERIALS

science.org/doi/10.1126/science.adz7969
Materials and Methods; Figs. S1 to S24; Tables S1 to S4

Submitted 15 June 2025; accepted 30 September 2025

10.1126/science.adz7969